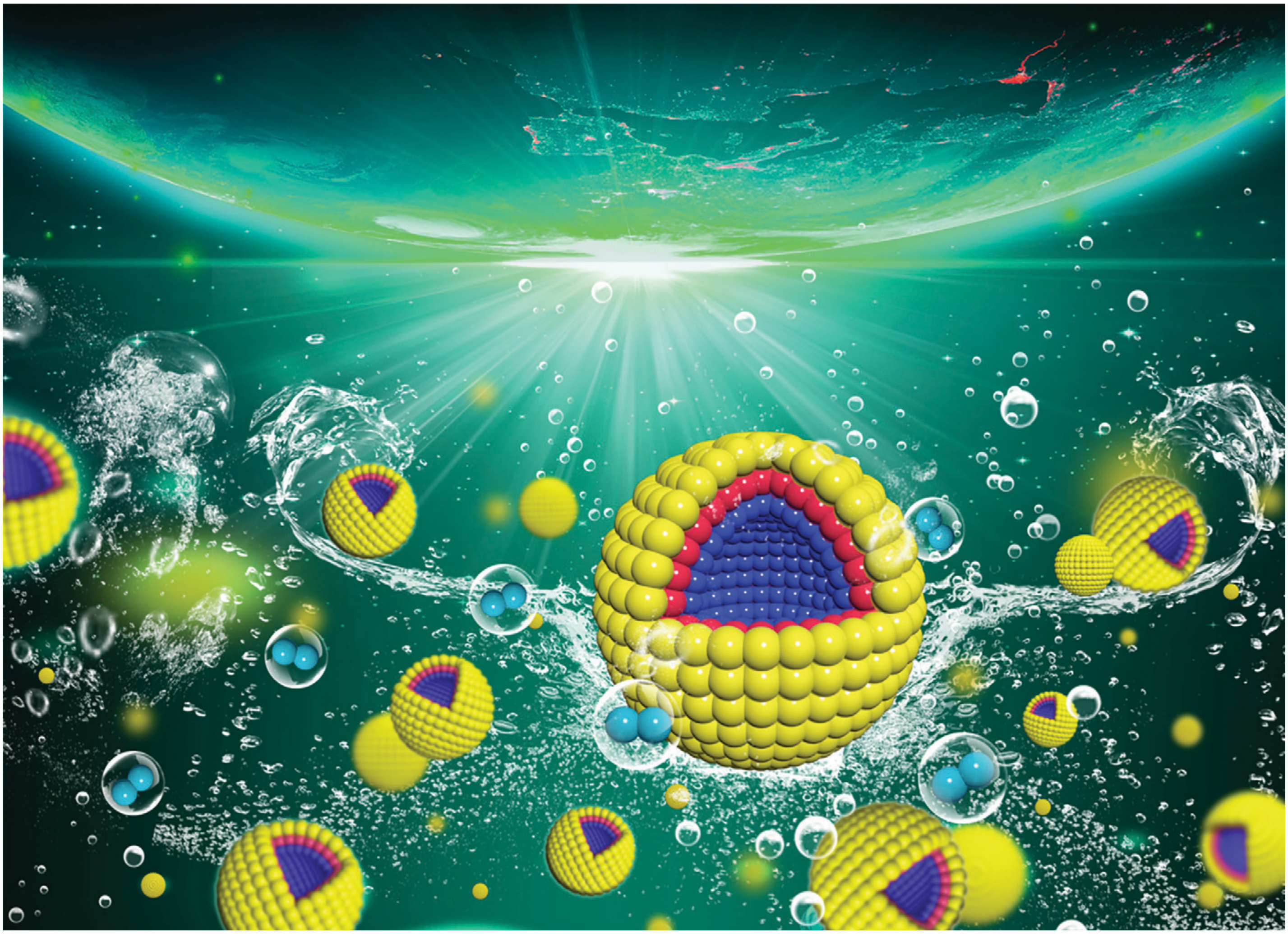

**Showcasing research from Prof. Zhao-Qing Liu's group at Guangzhou University in China. Image designed and illustrated by Ning-Chao Zheng.**

Ultrathin CdS shell-sensitized hollow S-doped $CeO_2$ spheres for efficient visible-light photocatalysis

By virtue of the reduced bandgap caused by the oxygen vacancies in the S-doped $CeO_2$, and the CdS sensitization effect accelerating the interface carrier separation and transfer, the $CeO_{2-x}S_x$@CdS composite exhibits superior photocatalytic activity for hydrogen evolution under visible light illumination.

## As featured in:

Catalysis Science & Technology

See Zhu Wang, Zhao-Qing Liu *et al.*, *Catal. Sci. Technol.*, 2019, **9**, 1357.

ROYAL SOCIETY OF CHEMISTRY | Celebrating IYPT 2019

rsc.li/catalysis

Catalysis Science & Technology

PAPER

Cite this: *Catal. Sci. Technol.*, 2019, **9**, 1357

# Ultrathin CdS shell-sensitized hollow S-doped $CeO_2$ spheres for efficient visible-light photocatalysis†

Ning-Chao Zheng,[ab] Ting Ouyang,[a] Yibo Chen,[a] Zhu Wang,*[ab] Di-Yun Chen[b] and Zhao-Qing Liu *[a]

Received 25th October 2018,
Accepted 23rd December 2018

DOI: 10.1039/c8cy02206b

rsc.li/catalysis

Highly efficient photocatalysts are urgently needed with the ever-increasing problems of environmental pollution and the energy crisis. Herein, we report a shape-controlled binary photocatalyst consisting of S-doped $CeO_2$ hollow spheres sensitized with ultrathin CdS shells. The core-shelled $CeO_{2-x}S_x$@CdS composite is synthesized using a simple template-assisted method followed by anion-exchange and chemical bath deposition processes. Owing to the reduced band gap caused by the oxygen vacancies in the S-doped $CeO_2$, and the CdS sensitization effect accelerating the interface carrier separation and transfer, the $CeO_{2-x}S_x$@CdS composite exhibits superior photocatalytic activity for hydrogen evolution (1147.2 μmol $g^{-1}$ $h^{-1}$) under visible-light illumination, which is 4.4, 11.1 and 94.8 times higher than that of CdS (258.2 μmol $g^{-1}$ $h^{-1}$), $CeO_{2-x}S_x$ (103.0 μmol $g^{-1}$ $h^{-1}$) and $CeO_2$ (12.1 μmol $g^{-1}$ $h^{-1}$), respectively. In addition, the composite displays highly efficient organic pollutant degradation (99.8% degradation of RhB within 25 min).

## 1. Introduction

Solar-driven photocatalysis as a green and sustainable technology is regarded as one of the most effective ways to address the energy- and environment-related issues.[1–5] Particularly, the photocatalytic $H_2$ evolution from water splitting driven by solar energy is highly attractive for converting solar energy to clean and renewable fuel.[6] In this regard, the key lies in the design and synthesis of suitable photocatalysts that can harvest sunlight, facilitate photo-generated charge carrier separation, and thus accelerate surface redox reaction.[7,8] To date, considerable progress has been made in developing heterojunction photocatalysts by coupling two or more active materials including oxides,[9] sulfides,[10,11] and nitrides[12] for hydrogen evolution reaction. However, further developing commercial and large-scale photocatalysts is still limited by their low activity and high cost.[13–15]

As a nontoxic, functional and abundant rare earth oxide, $CeO_2$ has gained much attention in catalysis, fuel cells, and gas sensors owing to its controlled morphology, good structural stability, and high oxygen storage capacity.[16–21] Notably, by virtue of the excellent redox potential between two oxidation states ($Ce^{3+} \rightarrow Ce^{4+}$), $CeO_2$ can easily modulate different nonstoichiometric compositions ($CeO_{2-x}$) with oxygen vacancies *via* anion doping.[22,23] Consequently, the oxygen vacancies can be easily formed, transferred and eliminated. This unique feature can greatly improve the surface adsorption of reactants and largely enhance electron transfer, further making $CeO_2$ a front-rank semiconductor photocatalyst.[24,25] However, the photocatalytic activity of $CeO_2$ in the visible-light region is still unsatisfactory due to its large band gap ($E_g$ = 2.9 eV) and low charge carrier separation efficiency.[26,27] Accordingly, many strategies including band gap engineering, morphology control, element doping, and surface modification have been developed to address these drawbacks.[28–30] Among these methods, sulfur doping is a feasible and effective strategy to broaden the visible light-responsive range and suppress the recombination of photoinduced electron–hole pairs, thus improving visible-light photocatalytic performance.[31,32] Unfortunately, it is still imperative to decorate and functionalize $CeO_{2-x}S_x$ owing to the slightly enhanced photocatalytic performance.

In addition, the construction of a hollow sphere structure with high specific surface area and atomic utilization efficiency is another approach to extend the visible light-responsive range and speed up the separation of photoinduced electrons and holes.[33,34] Cadmium sulfide (CdS) is an extensively employed photocatalyst because of its excellent band gap (~2.4 eV) and sensitizing properties, which can not

---

[a] *School of Chemistry and Chemical Engineering/Institute of Clean Energy and Materials/Key Laboratory for Water Quality and Conservation of the Pearl River Delta, Ministry of Education, Guangzhou University, Guangzhou 510006, China. E-mail: wangzhu@gzhu.edu.cn, lzqgzu@gzhu.edu.cn*

[b] *School of Environmental Science and Engineering/Guangdong Provincial Key Laboratory for Radionuclides Pollution Control and Resources, Guangzhou University, Guangzhou 510006, China*

† Electronic supplementary information (ESI) available. See DOI: 10.1039/c8cy02206b

only harvest visible light but also rapidly separate photoinduced electron–hole pairs.[35,36] Hence, it is highly desirable to design and develop a highly efficient and hollow photocatalyst by integrating the energy band-optimized $CeO_{2-x}S_x$ with a CdS sensitizer.

Herein, we present a "template + anion-exchange + chemical bath deposition" strategy for the fabrication of a shape-controlled photocatalyst composed of hollow S-doped $CeO_2$ sphere and ultrathin CdS shell. The main step of this synthesis is illustrated in Scheme 1: uniform $SiO_2$ spheres were firstly fabricated as the hard template and $CeO_2$ nanoparticles were decorated onto the surface of the $SiO_2$ spheres, followed by alkaline etching to obtain hollow $CeO_2$ spheres. Then, a simple anion-exchange process was employed for the preparation of $CeO_{2-x}S_x$. Finally, the $CeO_{2-x}S_x$@CdS composite was obtained by a chemical bath deposition method. Impressively, the $CeO_{2-x}S_x$@CdS composite exhibited significantly enhanced photocatalytic activity compared with the pristine semiconductors. The enhanced activity could be ascribed to the sulfur doping and the synergistic effect between the hollow $CeO_{2-x}S_x$ and CdS shell, which resulted in the extended visible-light absorption and improved interfacial carrier separation and transfer. These findings may provide new insight into designing and developing versatile photocatalyst materials with hollow structures for clean energy conversion and environmental pollutant degradation.

## 2. Experimental

### 2.1. Reagents

Cerium nitrate hexahydrate ($Ce(NO_3)_3·6H_2O$, ≥99.9%), cadmium nitrate tetrahydrate ($CdN_2O_6·4H_2O$, ≥99.0%), cadmium diacetate dehydrate ($Cd(Ac)_2·2H_2O$), thiourea ($CH_4N_2S$, ≥99.0%), sodium sulfide ($Na_2S·9H_2O$, ≥98.0%), sodium sulfite anhydrous ($Na_2SO_3$, ≥97.0%), sodium hydroxide (NaOH, ≥96.0%), rhodamine B (RhB, $C_{28}H_{31}ClN_2O_3$, ≥99.5%), ethyl silicate ($C_8H_{20}O_4Si$, AR), ethylene glycol ($(CH_2OH)_2$, AR), ammonium hydroxide ($NH_3·H_2O$, 25–28 wt%), and absolute ethanol (EtOH, AR) were purchased from Guangzhou Chemical Reagent Factory. All chemicals and reagents were of analytical grade and used without further purification.

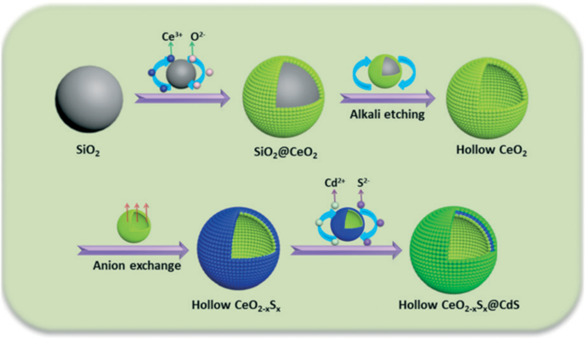

**Scheme 1** Schematic illustration for the synthesis of the $CeO_{2-x}S_x$@CdS composite.

### 2.2. Synthesis of hollow $CeO_{2-x}S_x$@CdS catalysts

**2.2.1. Preparation of $SiO_2$ template particles.** Uniform $SiO_2$ nanoparticles were synthesized *via* a facile method. Typically, a mixture solution of $C_8H_{20}O_4Si$ (10 mL) and EtOH (60 mL) was added dropwise into the mixture of $NH_3·H_2O$ (25–28 wt%, 8 mL) and EtOH (150 mL) with vigorous stirring within 30 min, and then the mixture was stirred for 24 h at 25 °C. The resulting sample was collected by centrifugation (8000 rpm, 10 min), and dried at 65 °C for 6 h.

**2.2.2. Preparation of $SiO_2$@$CeO_2$ and $CeO_2$ hollow spheres.** $SiO_2$@$CeO_2$ was prepared using a slightly modified method.[37] 300 mg of dried $SiO_2$ nanospheres were dispersed in 43 mL $(CH_2OH)_2$ with the assistance of ultrasound. Then, 1.0 g of $Ce(NO_3)_3·6H_2O$ and 3.5 mL of distilled water were added to the mixture and it was stirred vigorously for 30 min to form a homogeneous solution. The mixture was then transferred into a 250 mL round-bottom flask to undergo reflux condensation at 140 °C with stirring for 15 h. After the reaction vessel was cooled down to 25 °C, the precipitate ($SiO_2$@$CeO_2$) was separated by filtration and washed with distilled water and ethanol. To remove the $SiO_2$ cores, the $SiO_2$@$CeO_2$ samples were ultrasonically dispersed in 5 M NaOH for 24 h at 60 °C in a 250 mL round-bottom flask. Finally, the $CeO_2$ hollow spheres were obtained by filtration, washed with distilled water and ethanol, and dried in an oven at 80 °C overnight.

**2.2.3. Preparation of hollow $CeO_{2-x}S_x$ and $CeO_{2-x}S_x$@CdS catalysts.** The hollow $CeO_{2-x}S_x$ samples were synthesized by an anion exchange method. In detail, 200 mg of the dried $CeO_2$ hollow spheres were placed in a square combustion boat, while another square combustion boat was filled with 6.0 g of $CH_4N_2S$. Then, the two square combustion boats were transferred into a tube furnace with $CH_4N_2S$ loaded upstream and heated under a nitrogen flow at 500 °C for 2 h. The hollow $CeO_{2-x}S_x$@CdS nanocomposites were synthesized as follows: 0.05 M $CH_4N_2S$ + 0.05 M $CdN_2O_6·4H_2O$ were dissolved in 100 mL distilled water. To this, 100 mg of $CeO_{2-x}S_x$ was added. Then the mixture was transferred into a 250 mL round-bottom flask to undergo reflux condensation at 90 °C with stirring for 1 h. The resulting product was collected by filtration, washed with distilled water and ethanol, and dried in an oven at 80 °C for 6 h.

### 2.3. Characterization

The crystal phases of the samples were analyzed by X-ray diffraction (XRD, PANalytical, PW3040/60) with Cu Kα radiation ($\lambda$ = 1.5418 Å). The morphologies and structures of the samples were characterized with field emission scanning electron microscopy (FE-SEM, JEOLJSM-7001F) and transmission electron microscopy (TEM, JEM2010-HR). The UV-visible diffuse reflectance spectra (DRS) of the samples were examined with a Hitachi UV-3010 spectrophotometer using $BaSO_4$ as a reference. The steady-state/time-resolved photoluminescence emission spectra (345 nm excitation) were measured at room temperature with a fluorescence spectrophotometer (Edinburgh Instruments, FLSP-920). The Raman spectra were recorded with a Raman spectrometer (Bruker, VERTEX70). The detailed chemical composition of the samples was obtained by using X-ray photoelectron spectroscopy (XPS, ESCALab250). The surface areas were measured using a Micromeritics ASAP 2460 instrument (USA), and electron spin resonance (ESR) spectroscopy was performed on an EMXPlus-10/20 at 100 K.

## 3. Results and discussion

### 3.1. Structure and morphology studies

The X-ray diffraction (XRD) patterns of the $CeO_2$, $CeO_{2-x}S_x$ and $CeO_{2-x}S_x$@CdS composites are shown in Fig. 1. The pattern of $CeO_2$ with the characteristic peaks at $2\theta = 28.6°$, 33.1°, 47.5° and 56.3° were assigned to the (111), (200), (220) and (311) planes of the cubic fluorite $CeO_2$ (JCPDS 34-0394). Interestingly, it can be observed that the intensity of the diffraction peaks decreases considerably for $CeO_{2-x}S_x$. This result is mainly ascribed to the sulfur doping in the $CeO_2$ crystal structure, thereby reducing the crystallinity of $CeO_2$. The XRD peaks of the $CeO_{2-x}S_x$@CdS composite indicate the coexistence of S-doped $CeO_2$ and hexagonal CdS, and no other impurity diffraction peak was observed. The XRD results verified that the $CeO_{2-x}S_x$@CdS nanocomposite was successfully synthesised.

The morphology and microstructure of the samples were investigated by SEM and TEM. The $SiO_2$ nanospheres show a diameter of 250 nm (Fig. S1a†). Because of the abundant surface amidogen groups, $Ce^{3+}$ cations could be absorbed and then the $CeO_2$ particles were formed on the surface of the $SiO_2$ spheres (Fig. S1b†).[38] After removing the interior $SiO_2$ cores by alkaline etching, the hollow $CeO_2$ spheres with a diameter of 310 nm and rough surface were obtained. After sulfurization, the diameter of the hollow $CeO_2$ spheres slightly decreased and their surface became smooth (Fig. S1c–e†). After chemical bath deposition, the ultimate $CeO_{2-x}S_x$@CdS composite was obtained. As shown in Fig. 2a, the SEM image of the $CeO_{2-x}S_x$@CdS composite shows that the CdS nanoparticles were uniformly coated on the surface of the $CeO_{2-x}S_x$ hollow spheres. The sample is about 330 nm in diameter and the thickness of the CdS shell is about 10 nm. The morphology and structure of the $CeO_{2-x}S_x$@CdS composite were further analyzed by TEM. The results showed that the $CeO_{2-x}S_x$@CdS composite possesses an inner hollow structure (Fig. 2b). The magnified TEM image in Fig. 2c further demonstrates an intact hollow sphere structure, in which the shell thickness of $CeO_{2-x}S_x$@CdS is about 40 nm, and the radius is around 125 nm. From the HRTEM image of the $CeO_{2-x}S_x$@CdS composite (Fig. 2d), the lattice fringes with a d-spacing of 0.312 and 0.271 nm can be seen, corresponding to the spacing of the (111) and (200) planes of the cubic fluorite structured $CeO_2$, while the lattice fringes with a d-spacing of 0.359 nm match well with the (100) plane of hexagonal CdS. Meanwhile, the $CeO_{2-x}S_x$@CdS composite was analyzed by EDX mapping (Fig. 2e–h and S2†). The elemental maps indicate the uniform distribution of Ce, O, S and Cd in the shell of the hollow $CeO_{2-x}S_x$@CdS spheres, in line with that of the CdS nanoparticles homogeneously coated on the surface of the $CeO_{2-x}S_x$ hollow spheres.

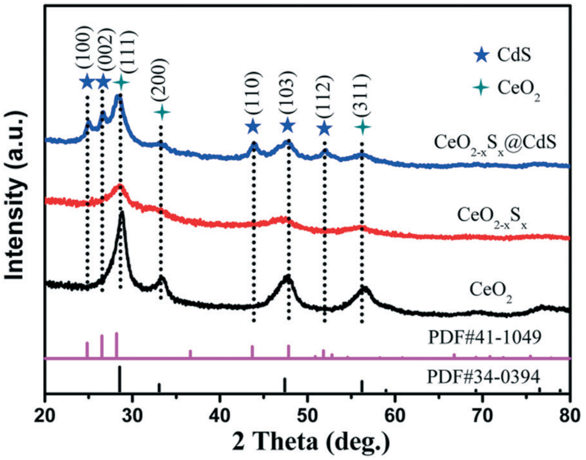

**Fig. 1** XRD patterns of the $CeO_2$, $CeO_{2-x}S_x$ and $CeO_{2-x}S_x$@CdS samples.

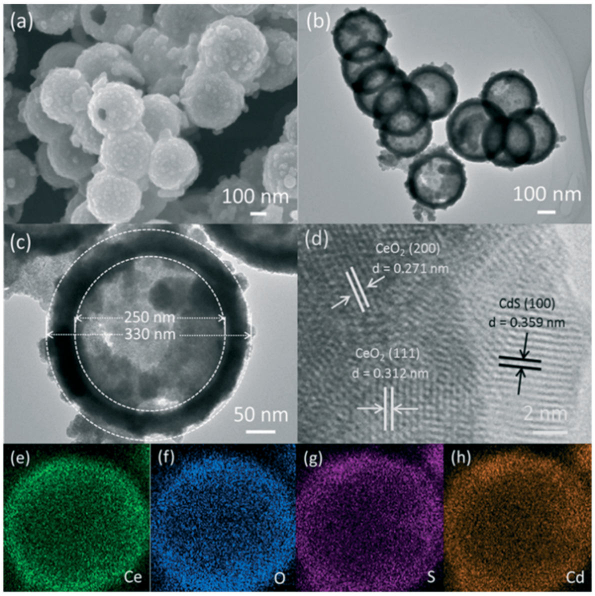

**Fig. 2** (a) SEM image, (b and c) TEM images, (d) HRTEM image, and (e–h) elemental mapping of the $CeO_{2-x}S_x$@CdS composite: (e) Ce, (f) O, (g) S and (h) Cd.

In addition, the surface areas of the samples were examined by nitrogen adsorption–desorption isotherms. The BET surface areas of $CeO_2$, $CeO_{2-x}S_x$, CdS and $CeO_{2-x}S_x$@CdS were calculated to be *ca.* 25.52, 27.42, 14.06 and 47.41 $m^2\ g^{-1}$, respectively (Fig. S3†). These results suggest that the coating of the thin CdS shell on the surface of $CeO_{2-x}S_x$ could effectively enhance the surface area. As a consequence, the more exposed active sites of the $CeO_{2-x}S_x$@CdS composite could be beneficial to improve the photocatalytic activity.

### 3.2. XPS analysis

X-ray photoelectron spectroscopy (XPS) was employed to analyze the elemental compositions and chemical states of the $CeO_2$, $CeO_{2-x}S_x$, and $CeO_{2-x}S_x$@CdS samples (Fig. S4†). Fig. 3a shows that the Ce 3d peak can be fitted into eight peaks, which can be assigned to $3d_{3/2}$ spin–orbit states (labeled u) and $3d_{5/2}$ states (labeled v).[39] The spectra of 885.1 eV (v′) and 904.4 eV (u′) assigned to $Ce^{3+}$ are observed, indicating the coexistence of $Ce^{3+}$ and $Ce^{4+}$ in the $CeO_{2-x}S_x$ and $CeO_{2-x}S_x$@CdS samples. This result suggests that the oxygen vacancies were formed in the $CeO_2$ lattice.[40] The quantitative analysis of the Ce 3d peak position is also summarized (Table S1†). The percentage of $Ce^{3+}$ ($Ce^{3+}$ species calculated based on the relative areas of the v′/u′ peaks according to the eqn S1†) is estimated to be ~27.8% for the $CeO_{2-x}S_x$@CdS samples. Therefore, the percentage of oxygen vacancies is ~13.9% in the region of the surface and sub-surface.[29] Moreover, the existence of oxygen vacancies was also investigated by electron spin resonance (ESR) spectroscopy (Fig. S5†). It can be clearly observed that the ESR signal of $CeO_2$ is a horizontal line. However, the $CeO_{2-x}S_x$ and $CeO_{2-x}S_x$@CdS samples exhibit a high intensity ESR signal peak at $g = 2.011$, which could be identified as the electrons trapped by the abundant oxygen vacancies, confirming the enhanced content of oxygen vacancies after S-doping and coating of the ultrathin CdS shell.[41] For the spectra of O 1s (Fig. 3b), the peak at 529.4 eV can be ascribed to the lattice oxygen in $CeO_2$, and another peak at 531.4 eV can be attributed to the adsorbed oxygen and adsorbed water on the surface.[42,43] Meanwhile, two broadened peaks of S 2p at around 161.7 eV (S $2p_{3/2}$) and 163.2 eV (S $2p_{1/2}$) are assigned to the sulfide ($S^{2-}$) (Fig. 3c).[44,45] The peaks centered at 405.1 eV (Cd $3d_{5/2}$) and 411.8 eV (Cd $3d_{3/2}$) are attributed to $Cd^{2+}$ in $CeO_{2-x}S_x$@CdS (Fig. 3d).[46,47]

### 3.3. Optical properties

The UV-vis diffuse reflectance spectra of the samples were measured to investigate their light absorption characteristics. The $CeO_2$ hollow spheres exhibit poor absorption of visible light and the absorption edge is around 420 nm (Fig. 4a), which is consistent with previous reports.[48,49] However, the $CeO_{2-x}S_x$ and $CeO_{2-x}S_x$@CdS samples exhibit extensively enhanced optical absorption with the edge extended to 540 nm and 560 nm, respectively (Fig. S6a and S7a†). One of the reasons is that the oxygen vacancies generated by the sulfur doping in $CeO_2$ could reduce the electronic band gap of $CeO_2$.[50] And another one is the sensitization of $CeO_{2-x}S_x$ by the deposited CdS shell.[26] These UV-vis diffuse reflectance spectra are also in accordance with the color evolution of the three samples (Fig. 4a, inset), in which the color of the samples turned from pale yellow to brown and finally to deep yellow with the sulfur doping and coating of the ultrathin CdS shell.

Raman spectroscopy was used to study the structural information of the samples. A strong Raman peak at ~460 $cm^{-1}$ is detected in the $CeO_2$ sample (Fig. 4b), which could be assigned to the $F_{2g}$ peak originating from the symmetrical stretching of the Ce–O vibrational unit in the fluorite-type structure.[51] Interestingly, the Raman peak of $CeO_{2-x}S_x$ shifted to a lower wavenumber compared to that of $CeO_2$. The shift can be attributed to the increased oxygen vacancies in the crystalline structure caused by S-doping.[22] Moreover, it can be seen that the $CeO_{2-x}S_x$@CdS nanocomposite shows two strong Raman peaks at ~300 and ~600 $cm^{-1}$, which are assigned to the first-order and second-order transverse optical phonon modes, respectively.[52]

In order to estimate the charge recombination and migration efficiency of the samples, photoluminescence (PL) measurements were carried out under 345 nm wavelength excitation. $CeO_2$ has a strong PL emission peak at around 410 nm (Fig. 4c), which may be attributed to the defect levels localized between

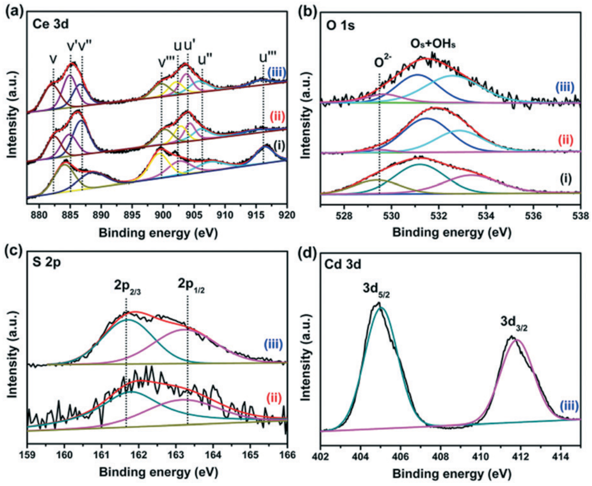

**Fig. 3** High-resolution XPS spectra of (a) Ce 3d, (b) O 1s, (c) S 2p and (d) Cd 3d; (i), (ii) and (iii) represent $CeO_2$, $CeO_{2-x}S_x$, and $CeO_{2-x}S_x$@CdS, respectively.

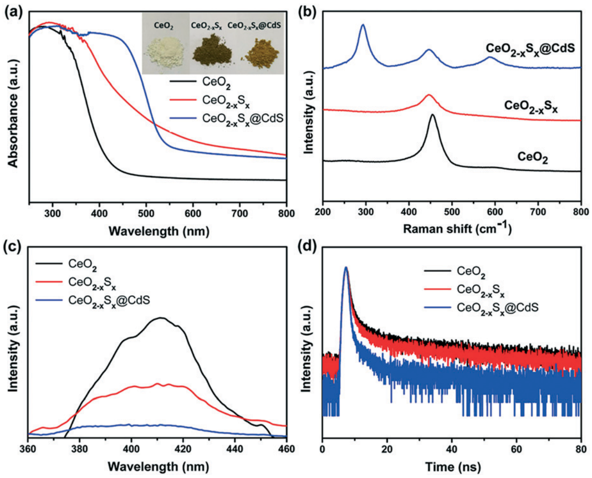

**Fig. 4** (a) UV-visible diffuse reflectance absorption spectra, (b) Raman spectra, (c) photoluminescence spectra, and (d) TRPL spectra of the $CeO_2$, $CeO_{2-x}S_x$ and $CeO_{2-x}S_x$@CdS samples.

the O 2p and Ce 4f levels.[53,54] As a comparison, the peak intensities of all the samples could be listed as follows: $CeO_2 > CeO_{2-x}S_x > CeO_{2-x}S_x$@CdS, indicating that $CeO_{2-x}S_x$@CdS possesses the lowest recombination rate of photoinduced electrons and holes. The time-resolved PL (TRPL) decay spectra further prove this conclusion. The TRPL spectra were fitted with a biexponential function and yield a short lifetime component ($\tau_1$) and long lifetime component ($\tau_2$) (Fig. 4d), and an average PL lifetime ($\tau$) was computed for comparison (Table S2†).[55,56] Significantly, the average PL lifetime of $CeO_{2-x}S_x$@CdS is 8.031 ns, which is shorter than that of $CeO_{2-x}S_x$ (15.182 ns) and $CeO_2$ (17.369 ns). This indicates that the introduction of S species and the coating of the ultrathin CdS shell can effectively enhance charge transfer and separation.[57]

### 3.4. Photoelectrochemical performance evaluation

Photoelectrochemical measurements of the as-prepared materials were conducted in an aqueous electrolyte with 0.25 M $Na_2S$ and 0.35 M $Na_2SO_3$. Fig. 5a shows the linear sweep voltammetry curves of the samples under visible-light illumination in the potential range of −1.0 to 1.2 V (*vs.* Ag/AgCl). It can be seen that $CeO_{2-x}S_x$@CdS exhibits a high response current density (6.93 mA $cm^{-2}$) compared with $CeO_2$ (2.05 mA $cm^{-2}$), $CeO_{2-x}S_x$ (3.31 mA $cm^{-2}$) and CdS (4.95 mA $cm^{-2}$) at 1.2 V. The transient photocurrents were measured under visible-light irradiation and at a voltage of 0.4 V by switching the light on/off and the results are presented in Fig. 5b. It can be observed that $CeO_2$ exhibited almost no response under visible-light irradiation. In contrast, the photocurrent density of $CeO_{2-x}S_x$@CdS is 8.65 μA $cm^{-2}$, which is much higher than that of $CeO_2$ (0.19 μA $cm^{-2}$), $CeO_{2-x}S_x$ (0.91 μA $cm^{-2}$) and CdS (2.64 μA $cm^{-2}$).

In addition, Mott–Schottky measurement provides another way to illustrate the enhanced photoelectrochemical activity. All the samples display positive slopes, indicating their n-type semiconductor nature (Fig. 5c).[58] Furthermore, the electrochemical impedance spectra (EIS) were recorded to determine the charge transfer properties (Fig. 5d). The Nyquist plots of the samples were measured at 0.6 V bias under visible-light irradiation, in which the semicircles of the Nyquist plots gradually reduce in the following sequence: $CeO_2 > CeO_{2-x}S_x >$ CdS $> CeO_{2-x}S_x$@CdS, reflecting the faster electron transfer process in $CeO_{2-x}S_x$@CdS (Fig. S6b and S7b†). Therefore, the enhanced photoelectrochemical performance of $CeO_{2-x}S_x$@CdS could be ascribed to the doping of sulfur to reduce the band gap of $CeO_2$ and the synergistic effect between the hollow $CeO_{2-x}S_x$ and ultrathin CdS shell, which effectively improve the optical absorption in the visible light range and suppress the recombination of photoinduced electron–hole pairs.

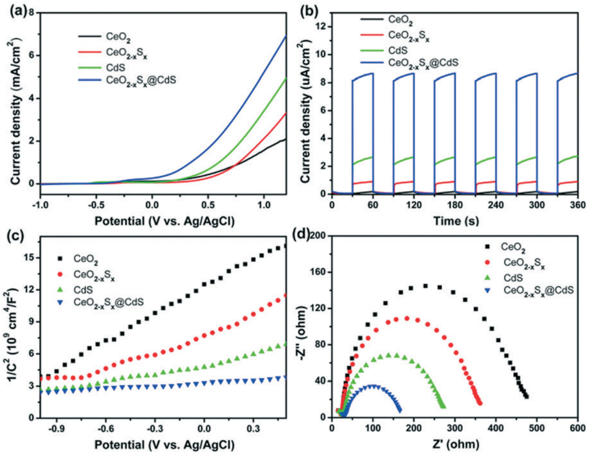

**Fig. 5** (a) Linear sweep voltammetry and (b) photocurrent response measurements of the $CeO_2$, $CeO_{2-x}S_x$, CdS and $CeO_{2-x}S_x$@CdS samples under visible-light irradiation ($\lambda > 420$ nm) and at a voltage of 0.4 V. (c) Mott–Schottky plots and (d) EIS Nyquist plots of the $CeO_2$, $CeO_{2-x}S_x$, CdS and $CeO_{2-x}S_x$@CdS samples.

### 3.5. Hydrogen evolution performance and mechanism analysis

Photocatalytic $H_2$ generation activities over the as-prepared photocatalysts were evaluated under visible-light illumination ($\lambda > 420$ nm) with a mixed solution (0.25 M $Na_2S$ + 0.35 M $Na_2SO_3$) as the hole sacrificial agents. It is clearly seen that the $CeO_2$ hollow spheres show very poor $H_2$ evolution activity due to their intrinsic drawbacks (Fig. 6a). However, with the doping of sulfur and coating of the ultrathin CdS shell, the photocatalytic $H_2$ evolution activity significantly increased. The $CeO_{2-x}S_x$@CdS composite exhibits excellent $H_2$ evolution activity with a rate of up to 1147.2 μmol $g^{-1}$ $h^{-1}$, which is much higher than that of $CeO_2$ (12.1 μmol $g^{-1}$ $h^{-1}$), $CeO_{2-x}S_x$ (103.0 μmol $g^{-1}$ $h^{-1}$), CdS (258.2 μmol $g^{-1}$ $h^{-1}$) and many other photocatalysts (Fig. S6d and S7d and Table S3†). These results suggest that the doping of sulfur and coating of the ultrathin CdS shell played critical roles in enhancing the photocatalytic $H_2$ generation activity. This is because the doping of sulfur could produce oxygen vacancies to reduce the band gap of $CeO_2$, and the coating of the ultrathin CdS shell could not only generate sensitization but also enlarge the surface area to increase the contact between the catalyst and reactant. Moreover, the photogenerated electrons in the conduction band of $CeO_{2-x}S_x$ could be easily transferred to the surface of CdS owing to their intimate interaction, which prevents the recombination of electron–hole pairs generated by $CeO_{2-x}S_x$. The photocatalytic

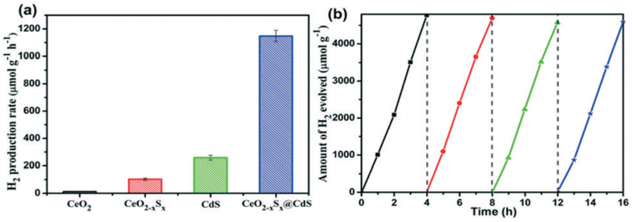

**Fig. 6** (a) Comparison of the $H_2$ evolution rate of $CeO_2$, $CeO_{2-x}S_x$, CdS and $CeO_{2-x}S_x$@CdS photocatalysts and (b) stability test of $H_2$ evolution for $CeO_{2-x}S_x$@CdS under visible-light irradiation ($\lambda > 420$ nm).

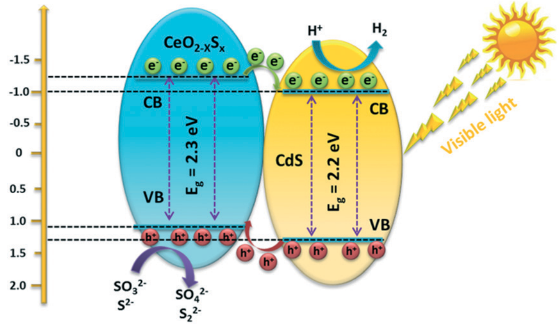

**Scheme 2** Schematic diagram of the proposed charge carrier transfer and $H_2$ evolution mechanism over the $CeO_{2-x}S_x$@CdS photocatalyst under visible-light irradiation.

degradation of the rhodamine B (RhB) dye was also tested with $CeO_{2-x}S_x$@CdS, and the degradation efficiency reached 99.8% within 25 min (Fig. S6c, S7c, S8, and S9†), which is superior to the performance of $CeO_2$, $CeO_{2-x}S_x$, and CdS under the same conditions. The stability of the $CeO_{2-x}S_x$@CdS photocatalysts for $H_2$ evolution was tested for 4 cycles, and the $CeO_{2-x}S_x$@CdS exhibited negligible attenuation in the prolonged photocatalytic testing (Fig. 6b and S10†).

Based on the above material characterization and visible-light photocatalytic activity of the $CeO_{2-x}S_x$@CdS photocatalyst, a possible mechanism for photocatalytic $H_2$ evolution over the $CeO_{2-x}S_x$@CdS photocatalyst is proposed (Scheme 2). The band gap of $CeO_{2-x}S_x$ and CdS was calculated to be 2.3 eV and 2.2 eV, respectively (Fig. S11a and S11b†). The flat band potential of $CeO_{2-x}S_x$ and CdS was calculated to be −1.2 eV and −1.0 eV according to the Mott–Schottky plots, respectively (Fig. S11c and S11d†). It is well known that the flat band potential is close to the conduction band in an n-type semiconductor.[59] Accordingly, the valance band position of $CeO_{2-x}S_x$ and CdS was calculated to be 1.1 eV and 1.2 eV, respectively. Thus, the CB position of $CeO_{2-x}S_x$ is more negative than that of CdS, and it ensures that the photoexcited donor level is energetically higher. Under visible-light irradiation, $CeO_{2-x}S_x$ absorbs photons and generates electro-hole pairs, and then the electrons from the CB of $CeO_{2-x}S_x$ migrate to the low energetic CB of CdS. On the surface of CdS, the adsorbed $H^+$ ions are reduced to $H_2$ by the electrons, while the holes accumulated at the surface are quenched by $SO_3^{2-}/S^{2-}$. The excellent visible-light photocatalytic activity of $CeO_{2-x}S_x$@CdS could be ascribed to the introduced oxygen vacancies that create defect energy levels in the band gap and effectively facilitate the interface electron transfer, resulting in the electron transfer process being faster than the recombination of photoinduced electron–hole pairs between the CB and VB of $CeO_{2-x}S_x$.

## 4. Conclusion

In summary, the shape-controlled S-doped $CeO_2$ hollow sphere decorated with an ultrathin CdS shell as a novel composite photocatalyst has been successfully fabricated by a "template + anion-exchange + chemical bath deposition" strategy. The photocatalytic activity could be remarkably improved by sulfur doping and the sensitization of ultrathin CdS shells. The $CeO_{2-x}S_x$@CdS composite exhibits excellent photocatalytic activity for both $H_2$ evolution and organic pollutant degradation, which could be explained as follows: i) the doping of sulfur species into the $CeO_2$ crystal structure can generate oxygen vacancies and reduce the band gap of the semiconductor; ii) the coating of the ultrathin CdS shell not only leads to the sensitization effect but also provides a large surface area and abundant active sites for the adsorption of reactants; iii) the composite structure of $CeO_{2-x}S_x$@CdS can promote the transfer of photogenerated electrons of $CeO_{2-x}S_x$ to the surface of CdS, thus hindering the recombination of the generated electron–hole pairs. Therefore, it is expected that the as-fabricated $CeO_{2-x}S_x$@CdS nanocomposite could open a new avenue to design advanced photocatalysts for clean energy generation and environmental remediation.

## Conflicts of interest

There are no conflicts to declare.

## Acknowledgements

This research was financially supported by the Natural Science Foundation of China (Grant No. 21875048, 21576056, and 21576057), the Natural Science Foundation of Guangdong Province (Grant No. 2017A030311016), the Science and Technology Research Project of Guangdong Province (Grant No. 2016A010103043), the Major Scientific Project of Guangdong University (Grant No. 2017KZDXM059), the Science and Technology Research Project of Guangzhou (Grant No. 201607010232), and Guangzhou University's 2017 Training Program for Young Top-Notch Personnel (BJ201704).

## Notes and references

1 X. B. Chen, L. Liu and F. Q. Huang, *Chem. Soc. Rev.*, 2015, **44**, 1861–1885.
2 X. J. Lang, J. C. Zhao and X. D. Chen, *Chem. Soc. Rev.*, 2016, **45**, 3026–3038.
3 Y. M. Shi and B. Zhang, *Chem. Soc. Rev.*, 2016, **45**, 1529–1541.
4 N. N. Meng, J. Ren, Y. Liu, Y. Huang, T. Petit and B. Zhang, *Energy Environ. Sci.*, 2018, **11**, 566–571.
5 O. Stroyuk, A. Raevskaya and N. Gaponik, *Chem. Soc. Rev.*, 2018, **47**, 5354–5422.
6 J. Liu, Y. Liu, N. Y. Liu, Y. Z. Han, X. Zhang, H. Huang, Y. Lifshitz, S. T. Lee, J. Zhong and Z. H. Kang, *Science*, 2015, **347**, 970–974.
7 D. Liu, J. Wang, X. J. Bai, R. L. Zong and Y. F. Zhu, *Adv. Mater.*, 2016, **28**, 7284–7290.
8 M. Zhu, Z. Sun, M. Fujitsuka and T. Majima, *Angew. Chem., Int. Ed.*, 2018, **57**, 2160–2164.

9 M. Zhu, X. Cai, M. Fujitsuka, J. Zhang and T. Majima, *Angew. Chem., Int. Ed.*, 2017, **56**, 2064–2068.

10 P. Y. Kuang, P. X. Zheng, Z. Q. Liu, J. L. Lei, H. Wu, N. Li and T. Y. Ma, *Small*, 2016, **12**, 6735–6744.

11 R. Shi, H. F. Ye, F. Liang, Z. Wang, K. Li, Y. X. Weng, Z. S. Lin, W. F. Fu, C. M. Che and Y. Chen, *Adv. Mater.*, 2018, **30**, 1705941–1705947.

12 D. Zheng, X.-N. Cao and X. Wang, *Angew. Chem., Int. Ed.*, 2016, **55**, 11512–11516.

13 C. M. Magdalane, K. Kaviyarasu, J. J. Vijaya, B. Siddhardha and B. Jeyaraj, *J. Photochem. Photobiol., B*, 2016, **163**, 77–86.

14 C. M. Magdalane, K. Kaviyarasu, J. J. Vijaya, C. Jayakumar, M. Maaza and B. Jeyaraj, *J. Photochem. Photobiol., B*, 2017, **169**, 110–123.

15 K. Kasinathan, J. Kennedy, M. Elayaperumal, M. Henini and M. Malik, *Sci. Rep.*, 2016, **6**, 38064–38076.

16 T. Montini, M. Melchionna, M. Monai and P. Fornasiero, *Chem. Rev.*, 2016, **116**, 5987–6041.

17 J. A. Rodriguez, D. C. Grinter, Z. Liu, R. M. Palomino and S. D. Senanayake, *Chem. Soc. Rev.*, 2017, **46**, 1824–1841.

18 J. Paier, C. Penschke and J. Sauer, *Chem. Rev.*, 2013, **113**, 3949–3985.

19 C. M. Magdalane, K. Kaviyarasu, J. J. Vijaya, B. Siddhardha, B. Jeyaraj, J. Kennedy and M. Maaza, *J. Alloys Compd.*, 2017, **727**, 1324–1337.

20 P. I. Rajan, J. J. Vijaya, S. K. Jesudoss, K. Kaviyarasu, S. C. Lee, L. J. Kennedy, R. Jothiramalingam, H. A. Al-Lohedan and M. M. Abdullah, *R. Soc. Open Sci.*, 2018, **5**, 171430–171439.

21 K. Kaviyarasu, E. Manikandan, Z. Y. Nuru and M. Maaza, *Mater. Lett.*, 2015, **160**, 61–63.

22 Y. T. Xiao, Y. J. Chen, Y. Xie, G. H. Tian, S. E. Guo, T. R. Han and H. G. Fu, *Chem. Commun.*, 2016, **52**, 2521–2524.

23 H. J. Jung, S. H. Kye, H. J. Kang, H. J. Yang, J. B. Yoo, K. H. Lee and N. H. Hur, *Appl. Catal., A*, 2018, **558**, 9–17.

24 T. Ye, W. M. Huang, L. M. Zeng, M. L. Li and J. L. Shi, *Appl. Catal., B*, 2017, **210**, 141–148.

25 S. L. Xie, Z. L. Wang, F. L. Cheng, P. Zhang, W. J. Mai and Y. X. Tong, *Nano Energy*, 2017, **34**, 313–337.

26 S. Sultana, S. Mansingh, M. Scurrell and K. M. Parida, *Inorg. Chem.*, 2017, **56**, 12297–12307.

27 J.-J. Li, E.-Q. Yu, S.-C. Cai, X. Chen, J. Chen, H.-P. Jia and Y.-J. Xu, *Appl. Catal., B*, 2018, **240**, 141–152.

28 W. X. Zou, B. Deng, X. X. Hu, Y. P. Zhou, Y. Pu, S. H. Yu, K. L. Ma, J. F. Sun, H. Q. Wan and L. Dong, *Appl. Catal., B*, 2018, **238**, 111–118.

29 W. Y. Lei, T. T. Zhang, L. Gu, P. Liu, J. A. Rodriguez, G. Liu and M. H. Liu, *ACS Catal.*, 2015, **5**, 4385–4393.

30 A. D. Liyanage, S. D. Perera, K. Tan, Y. Chabal and K. J. Balkus, *ACS Catal.*, 2014, **4**, 577–584.

31 T. Q. Lin, C. Y. Yang, Z. Wang, H. Yin, X. J. Lü, F. Q. Huang, J. H. Lin, X. M. Xie and M. H. Jiang, *Energy Environ. Sci.*, 2014, **7**, 967–972.

32 C. Z. Sun, H. Zhang, H. Liu, X. X. Zheng, W. X. Zou, L. Dong and L. Qi, *Appl. Catal., B*, 2018, **235**, 66–74.

33 B. Liu, L. M. Liu, X. F. Lang, H. Y. Wang, X. W. Lou and E. S. Aydil, *Energy Environ. Sci.*, 2014, **7**, 2592–2597.

34 Y. S. Si, M. Chen and L. M. Wu, *Chem. Soc. Rev.*, 2016, **45**, 690–714.

35 R. B. Wei, Z. L. Huang, G. H. Gu, Z. Wang, L. X. Zeng, Y. B. Chen and Z. Q. Liu, *Appl. Catal., B*, 2018, **231**, 101–107.

36 Q. Wu, H. F. Zhao, F. Huang, J. Hou, H. B. Cao, Z. Y. Liu, S. L. Peng and G. Z. Cao, *J. Phys. Chem. C*, 2017, **121**, 18430–18438.

37 N. Li, H. Y. Zhao, Y. Zhang, Z. Q. Liu, X. Y. Gong and Y. P. Du, *CrystEngComm*, 2016, **18**, 4158–4164.

38 X. Gong, Y. Q. Gu, N. Li, H. Zhao, C. J. Jia and Y. Du, *Inorg. Chem.*, 2016, **55**, 3992–3999.

39 B. Xu, Q. T. Zhang, S. S. Yuan, M. Zhang and T. Ohno, *Appl. Catal., B*, 2016, **183**, 361–370.

40 Z. Q. Cui, W. K. Wang, C. J. Zhao, C. Chen, M. M. Han, G. Z. Wang, Y. X. Zhang, H. M. Zhang and H. J. Zhao, *ACS Appl. Mater. Interfaces*, 2018, **10**, 31394–31403.

41 A. Naldoni, M. Allieta, S. Santangelo, M. Marelli, F. Fabbri, S. Cappelli, C. L. Bianchi, R. Psaro and V. D. Santo, *J. Am. Chem. Soc.*, 2012, **134**, 7600–7603.

42 N. Zhang, X. Y. Li, H. C. Ye, S. M. Chen, H. X. Ju, D. B. Liu, Y. Lin, W. Ye, C. M. Wang, Q. Xu, J. F. Zhu, L. Song, J. Jiang and Y. J. Xiong, *J. Am. Chem. Soc.*, 2016, **138**, 8928–8935.

43 B. Hillary, P. Sudarsanam, M. H. Amin and S. K. Bhargava, *Langmuir*, 2017, **33**, 1743–1750.

44 Z. J. Tan, P. R. Liu, H. M. Zhang, Y. Wang, M. Al-Mamun, H. G. Yang, D. Wang, Z. Y. Tang and H. J. Zhao, *Chem. Commun.*, 2015, **51**, 5695–5697.

45 S. S. Gu, Y. N. Chen, X. Z. Yuan, H. Wang, X. H. Chen, Y. Liu, Q. Jiang, Z. B. Wu and G. M. Zeng, *RSC Adv.*, 2015, **5**, 79556–79564.

46 N. Zhang, S. Xie, B. Weng and Y.-J. Xu, *J. Mater. Chem. A*, 2016, **4**, 18804–18814.

47 B. C. Qiu, Q. H. Zhu, M. M. Du, L. G. Fan, M. Y. Xing and J. L. Zhang, *Angew. Chem., Int. Ed.*, 2017, **56**, 2684–2688.

48 X. J. Wen, C. G. Niu, L. Zhang, C. Liang and G. M. Zeng, *Appl. Catal., A*, 2018, **221**, 701–714.

49 N. Tian, H. W. Huang, C. Y. Liu, F. Dong, T. R. Zhang, X. Du, S. X. Yu and Y. H. Zhang, *J. Mater. Chem. A*, 2015, **3**, 17120–17129.

50 J. S. Zhang, J. H. Sun, K. Maeda, K. Domen, P. Liu, M. Antonietti, X. Z. Fu and X. C. Wang, *Energy Environ. Sci.*, 2011, **4**, 675–678.

51 P. Sudarsanam, B. Mallesham, D. N. Durgasri and B. M. Reddy, *J. Ind. Eng. Chem.*, 2014, **20**, 3115–3121.

52 A. D. Mani, S. Nandy and C. Subrahmanyam, *J. Environ. Chem. Eng.*, 2015, **3**, 2350–2357.

53 L. Chen, D. W. Meng, X. L. Wu, A. Wang, J. X. Wang, Y. Q. Wang and M. H. Yu, *J. Phys. Chem. C*, 2016, **120**, 18548–18559.

54 J. Han, J. Meeprasert, P. Maitarad, S. Nammuangruk, L. Y. Shi and D. S. Zhang, *J. Phys. Chem. C*, 2016, **120**, 1523–1533.

55 X. Li, S. W. Liu, K. Fan, Z. Q. Liu, B. Song and J. G. Yu, *Adv. Energy Mater.*, 2018, **8**, 1800101–1800110.

56 S. Y. Chae, S. J. Park, S. G. Han, H. Jung, C. W. Kim, C. Jeong, O. S. Joo, B. K. Min and Y. J. Hwang, *J. Am. Chem. Soc.*, 2016, **138**, 15673–15681.

57 W. Q. Wei, D. Liu, Z. Wei and Y. F. Zhu, *ACS Catal.*, 2016, **7**, 652–663.

58 R. B. Wei, P. Y. Kuang, H. Cheng, Y. B. Chen, J. Y. Long, M. Y. Zhang and Z. Q. Liu, *ACS Sustainable Chem. Eng.*, 2017, **5**, 4249–4257.

59 Z. Zhang and J. T. Yates, *Chem. Rev.*, 2012, **112**, 5520–5551.